

Controlling UAVs by Sensing the Electric or the Magnetic Field Around Power Lines

Aykut C. Satici¹, Member, IEEE, Alex Peterson, John Chiasson, Life Fellow, IEEE, and Zachary Adams

Abstract—We provide a procedure for estimating the relative position of a drone with respect to three-phase power lines. This is done by making use of the root mean square (rms) measurements of the electric/magnetic fields emanating from the power lines. Maxwell's equations are used to derive the sensor measurement model showing that the total rms electric/magnetic field is a measure of the relative position of the drone. The squared inverse of the total rms electric/magnetic field serves as a potential function for a Hamiltonian, which in turn is a Lyapunov function. It is shown that the gradient of this potential function always points to the (convex hull of the) power lines. Based on Lyapunov analysis, a control algorithm is developed that forces a drone to follow the gradient of the potential to the power lines. This controller provides the capability to inspect power lines or carry out installation tasks on them. Simulations are presented to illustrate the efficacy of the approach.

Index Terms—Electrodynamics, state estimation, control.

I. INTRODUCTION

ROBOTIC automation has been expanding in scope over the last few decades. Many aspects of our everyday lives have been penetrated by service robots that improve the quality or efficiency by which certain tasks are performed. Efficient power distribution is another such area whose efficiency can be improved with the help of robotic agents, but this potential has yet to be exploited due to some technological gaps.

Power transmission and distribution through power lines are fundamentally limited by the amount of current a given power line can carry. This depends on several factors, but perhaps the most important is the weather environment around the power line. Currently, power companies rate the maximum current

using what called a static-line rating (SLR), which is a worst-case capacity for a power line, based on empirical seasonal temperature estimates without regard to instantaneous weather conditions, such as strong winds, which would help transfer heat from the power line into the surrounding air [1]. This observation hints at a simple conceptual solution to increasing the efficiency of power distribution: measure the instantaneous weather conditions around a power line at regular intervals to determine the amount of power allowed to flow through the wires. This concept may be realized by installing dynamic-line rating (DLR) sensors on power lines, which house an array of sensors, such as wind speed, ambient/line temperature, and line angle. They are powered by small solar panels or even through inductive charging once installed on a power line. These measurements are communicated back to power utilities, who then use this information to determine the amount of power which can be sent through the power lines.

Even though the DLR technology has been known to power engineers for a long time [2], [3], it has largely been underutilized until recently because of the cost and difficulty in installing DLR sensors. Helicopter installations are dangerous due to the necessity that they must hover at low altitude next to a live power line [4]. Fortunately, recent advances in drone technology provides an alternative method to autonomously place these sensors. As for any robotic manipulation task, this one requires accurate localization of the drone with respect to the power lines so that the drone can perform the installation task.

Conventional state estimation schemes, involving vision-based systems and time-of-flight sensors have difficulty in performing accurate localization as power lines have a small volumetric footprint. The video in [5] shows a DLR sensor being installed on a live power line at the Idaho National Laboratory by one of the authors (Z.A.). An additional video in [6] shows the first-person view of Z.A. installing a DLR sensor on another power line. It can be observed that the drone must approximately be within a foot from the power line for localization. Further, small noise in image formation can easily cause large localization errors since the cross-section of a power line occupies just a few pixels in a camera's image. Magnetometers will not work next to a power line. Furthermore, a GPS cannot provide the position of the UAV with respect to a power line. Instead of relying on conventional state-estimation modalities, we exploit the measurements of the electric and/or magnetic fields around power lines in order to perform localization. We develop a model of this

Manuscript received 24 August 2023; revised 20 October 2023; accepted 13 November 2023. Date of publication 21 November 2023; date of current version 6 December 2023. This work was supported by USDA SBIR under Grant 2023-33530-39244. Recommended by Senior Editor S. Dey. (Corresponding author: Aykut C. Satici.)

Aykut C. Satici and Alex Peterson are with the Mechanical and Biomedical Engineering Department, Boise State University, Boise, ID 83706 USA (e-mail: aykutsatici@boisestate.edu; alexpeterson841@boisestate.edu).

John Chiasson is with the Electrical and Computer Engineering Department, Boise State University, Boise, ID 83706 USA (e-mail: johnchiasson@boisestate.edu).

Zachary Adams is with Pitch Aeronautics, Boise, ID 83716 USA (e-mail: zachary.adams@pitchaero.com).

Digital Object Identifier 10.1109/LCSYS.2023.3334998

2475-1456 © 2023 IEEE. Personal use is permitted, but republication/redistribution requires IEEE permission.
See <https://www.ieee.org/publications/rights/index.html> for more information.

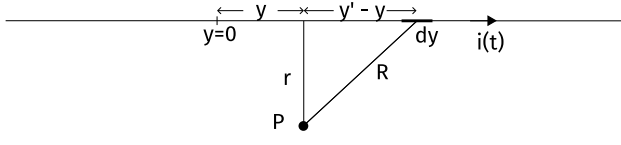


Fig. 1. Infinitely long wire carrying a sinusoidal current.

measurement, and use its properties to localize a drone with respect to the power line. Our method to estimate the drone's pose relative to a power line is based on measuring the total root mean square (rms) of the electric or magnetic field.

II. ELECTRIC AND MAGNETIC FIELDS

We start by computing the electric and magnetic fields emanating from one transmission line carrying an ac current of amplitude I_0 and angular frequency ω ($2\pi 60$ in the U.S.). In the subsequent subsection, we extend this computation by superposition to three-phase transmission lines.

A. Single-Phase Current

Let (r', ϕ', y') denote a source point and (r, ϕ, y) denote a point P at which we are seeking the electric and magnetic fields as shown in Figure 1. Note that the wire lies along the y -axis. The distance to the point P is therefore given by $R(r, y - y') = \sqrt{r^2 + (y' - y)^2}$.

The retarded time is defined as $t_R(y - y', t) \triangleq t - R/c$. The appropriate form of the current is given by the traveling wave

$$i(y, t) = I_0 e^{j(\omega t - \gamma y)},$$

where the propagation constant γ is given by $\gamma = \beta k$, with $k \triangleq \omega/c$, $1/2 \leq \beta < 1$ and c the speed of light [7], [8]. For convenience, define the function

$$f(r, y) \triangleq \frac{e^{-j(\omega/c \sqrt{r^2 + y^2} + \gamma y)}}{\sqrt{r^2 + y^2}}.$$

Following [9, ch. 10], the retarded vector potential at point P is given by

$$\begin{aligned} \mathbf{A}(r, y, t) &= A_y \hat{\mathbf{y}} = \frac{\mu_0}{4\pi} \hat{\mathbf{y}} \int_{-\infty}^{\infty} \frac{i(y', t_R)}{R} dy' \\ &= \frac{\mu_0 I_0}{4\pi} e^{j(\omega t - \gamma y)} \hat{\mathbf{y}} \int_{-\infty}^{\infty} f(r, y') dy'. \end{aligned} \quad (1)$$

The (complex) magnetic field is computed from the vector potential as follows [9]

$$\begin{aligned} \mathbf{B}(r, y, t) &= \nabla \times \mathbf{A}(r, t) = -\frac{\partial A_y}{\partial r} \hat{\boldsymbol{\phi}} = B_{\phi} \hat{\boldsymbol{\phi}} \\ &= -\frac{\mu_0 I_0}{4\pi} e^{j(\omega t - \gamma y)} \hat{\boldsymbol{\phi}} \int_{-\infty}^{\infty} \frac{\partial}{\partial r} f(r, y') dy'. \end{aligned}$$

With $\mathbf{B} \triangleq \text{Re}\{\mathbf{B}\}$, it follows from [10] that the above equation yields

$$\begin{aligned} \mathbf{B}(r, y, t) &= \frac{\mu_0 I_0 \zeta}{4} \hat{\boldsymbol{\phi}} [J_1(\zeta r) \sin(\omega t - \gamma y) \\ &\quad - Y_1(\zeta r) \cos(\omega t - \gamma y)], \end{aligned} \quad (2)$$

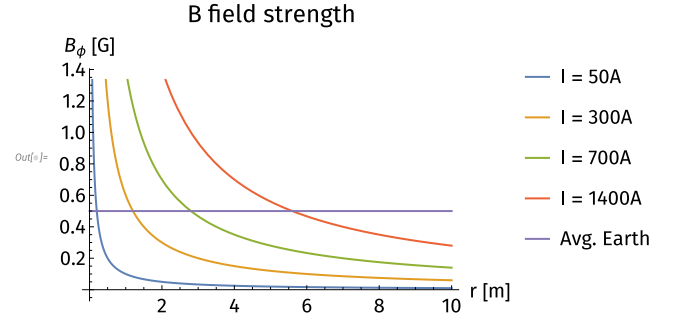


Fig. 2. Peak magnetic \mathbf{B} field strengths for various values of the current amplitude I_0 with $\omega = 2\pi 60 \text{ rad s}^{-1}$.

where $\zeta = \sqrt{k^2 - \gamma^2} = \omega/c \sqrt{1 - \beta^2} \leq \sqrt{3}\omega/2c$; J_1 and Y_1 are order 1 Bessel functions of the first and second kind, respectively. For $x \ll 1$, they are well-approximated by

$$J_1(x) \approx \frac{x}{2}, \quad Y_1(x) \approx -\frac{2}{\pi x} + \frac{x \log x/2}{\pi}. \quad (3)$$

With $\omega = 2\pi 60 \text{ rad s}^{-1}$, we have $\zeta < 1.09 \times 10^{-6}$. Substituting (3) into (2) and using the fact that ζ is small, the magnetic field reduces to the quasi-static approximation

$$\mathbf{B}_{qs}(r, y, t) = B_{qs,\phi}(r, y, t) \hat{\boldsymbol{\phi}} = \frac{\mu_0 I_0}{2\pi r} \cos(\omega t - \gamma y) \hat{\boldsymbol{\phi}}. \quad (4)$$

Ampere's law

$$\mu_0 \epsilon_0 \frac{\partial \mathbf{E}}{\partial t} = \nabla \times \mathbf{B} = -\frac{\partial B_{\phi}}{\partial z} \hat{\mathbf{r}} + \frac{1}{r} \frac{\partial (r B_{\phi})}{\partial r} \hat{\mathbf{y}} \quad (5)$$

is then used to solve for the electric field $\mathbf{E} = E_r \hat{\mathbf{r}} + E_y \hat{\mathbf{y}}$.

$$\begin{aligned} E_r &= \frac{I_0 \zeta \gamma}{4\omega \epsilon_0} [J_1(\zeta r) \sin(\omega t - \gamma y) - Y_1(\zeta r) \cos(\omega t - \gamma y)] \\ E_y &= -\frac{I_0 \zeta^2}{4\omega \epsilon_0} [J_0(\zeta r) \cos(\omega t - \gamma y) + Y_0(\zeta r) \sin(\omega t - \gamma y)]. \end{aligned} \quad (6)$$

The magnetic field is well-approximated using equations (3) so that $\mathbf{B} \approx \mathbf{B}_{qs}$ as given in equation (4). Using \mathbf{B}_{qs} in equation (5), we obtain the quasi-static approximation $\mathbf{E} \approx \mathbf{E}_{qs} = E_{qs,r} \hat{\mathbf{r}} + E_{qs,y} \hat{\mathbf{y}}$, with $E_{qs,y} = 0$ and

$$E_{qs,r} = \frac{\gamma I_0}{2\pi \epsilon_0 \omega r} \cos(\omega t - \gamma y) = \frac{\beta c \mu_0 I_0}{2\pi r} \cos(\omega t - \gamma y). \quad (7)$$

The peak strength of the magnetic field $\mathbf{B} = B_{\phi}(r) \hat{\boldsymbol{\phi}}$ at $\omega = 2\pi 60 \text{ rad s}^{-1}$ for various values of I_0 are plotted in Figure 2. The strength of the electric field $E_r(r)$ is just a scaled version of this plot by the factor βc . The directions of the quasi-static electric and magnetic fields are depicted in Figure 3.

The root-mean-squared (rms) magnitude of the electric and magnetic fields are easily computed as

$$\bar{E}_{qs,r} = \frac{\beta c \mu_0 I_0}{2\sqrt{2}\pi r}, \quad \bar{B}_{qs,\phi} = \frac{\mu_0 I_0}{2\sqrt{2}\pi r}. \quad (8)$$

B. Three-Phase Current

The currents in the power line form a balanced three-phase set for which a sample irregular geometry is shown in Figure 4. We compute the rms electric and magnetic field at an arbitrary

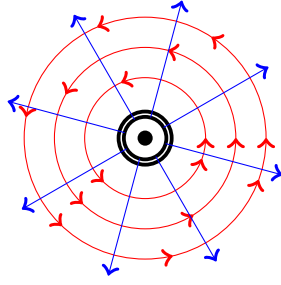


Fig. 3. Electric \mathbf{E} (blue) and magnetic \mathbf{B} (red) fields generated by the sinusoidal current through the wire.

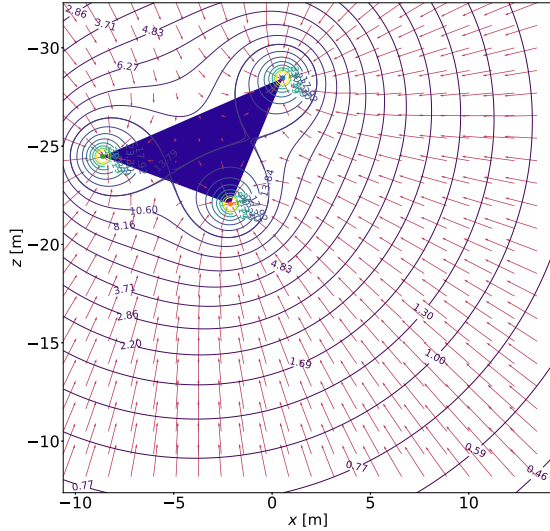


Fig. 4. Contour plot of the rms magnitude of the electric field for three-phase power line. The contour labels are the values of the rms electric field magnitude in kV. The vectors in the figure depict the gradient vector field of $1/\bar{E}^2$.

point P in space by superposing the fields generated by each individual transmission line, i.e.,

$$\bar{E} = \sqrt{\frac{\omega}{2\pi} \int_0^{2\pi/\omega} \left(\sum_{\alpha=1}^3 E_{qs,\alpha} \right)^2 dt}, \quad (9)$$

where

$$E_{qs,\alpha} = \frac{\gamma I_0}{2\pi \epsilon_0 \omega r_\alpha} \cos(\omega t - \gamma y_\alpha + 2\pi(\alpha - 1)/3).$$

As shown in [9, pg. 442], the time-average (rms) energy density, $\langle u \rangle$, of the electromagnetic field may be written as

$$\langle u \rangle = \frac{1}{2} \epsilon_0 \bar{E}^2 = \frac{1}{2\mu_0} \bar{B}^2, \quad (10)$$

where \bar{B} is the total rms magnetic field, computed similarly as in equation (9). The resulting rms electric field, \bar{E} , is shown in Figure 4 as a contour plot. From equation (10), $\bar{B} = \sqrt{\mu_0 \epsilon_0} \bar{E}$, showing that the contour curves for the rms magnetic field are the same as those of \bar{E} . The vectors in the plot indicate the negative gradient of $1/\bar{E}^2$.

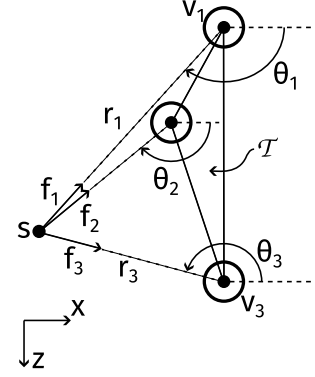


Fig. 5. Power line geometry: $r_\alpha = \xi/e_\alpha$ is the distance from power line v_α to the sensor s . θ_α is the angle the unit vector $-f_\alpha$ from v_α to s makes with the world's x -axis. \mathcal{T} is the triangle formed by the three wires.

III. PROBLEM DESCRIPTION

As discussed in Section I, the problem is to guide the UAV to the power lines where the use of conventional sensing modalities, such as magnetometers, vision systems, time-of-flight sensors, etc. is not practical. Our approach is motivated by Figure 4, which shows that starting from any point in the plane a UAV may be guided to the power lines by following the gradient of the rms electric/magnetic field.

We set the problem up in this section, beginning with the geometry of the sensor and the three-phase power lines. We assume that the world \hat{y} -axis coincides with the axial direction of the power lines. Figure 5, therefore, shows the power lines in the $\mathbf{q} = (x, z)$ -plane.

The sensor is depicted by s in this figure, and has the coordinates (x, z) in the plane. In Figure 5, the power lines are denoted by $\{v_\alpha\}_{\alpha=1}^3$ and their coordinates in the world frame are given by $\{(x_\alpha, z_\alpha)\}_{\alpha=1}^3$. From Section II, the distance from the wire v_α to the sensor s is r_α , which is inversely proportional to the peak electric field magnitude

$$e_\alpha = \frac{\xi}{r_\alpha} := \frac{\beta c \mu_0 I_0}{2\pi} \frac{1}{r_\alpha}, \quad \alpha = 1, 2, 3. \quad (11)$$

Let \hat{f}_α denote the unit vector from the sensor s to the wire v_α . We define θ_α to be the angle between the world's x -axis and the unit vector $-\hat{f}_\alpha$. The triangle formed by the three wires is denoted by \mathcal{T} (see Figure 5).

By the development in Section II, the electric field at the sensor s due to the wire α is given by

$$\mathbf{E}_\alpha(x, z, t) = e_\alpha \cos(\omega t - \gamma y + (\alpha - 1)2\pi/3) \begin{bmatrix} c_\alpha \\ -s_\alpha \end{bmatrix}.$$

The total electric field \mathbf{E} is the sum over $\alpha = 1, 2, 3$ of \mathbf{E}_α . Note that, in the (x, z) -coordinate system, $\hat{f}_\alpha := [-c_\alpha \ s_\alpha]^\top$, where $c_\alpha = \cos \theta_\alpha$ and $s_\alpha = \sin \theta_\alpha$. The dependence of \mathbf{E}_α on (x, z) is made apparent by noting that $x - x_\alpha = r_\alpha c_\alpha$ and $z - z_\alpha = -r_\alpha s_\alpha$.

With this set-up, our problem is to devise an estimation/control strategy that utilizes the rms electric or magnetic field that will take a UAV from an arbitrary point in the (x, z) -space to one of the power wires in order to install a sensor. We assume that we are able to align the UAV's body \hat{y} -axis axially with the wire. This may be achieved by having an

separate control system that regulates the yaw rotation to force the UAV's body $\hat{\mathbf{y}}$ -axis to align with the Poynting vector, $\mathbf{P} = 1/\mu_0 \mathbf{E} \times \mathbf{B}$, which must point along the power line (world $\hat{\mathbf{y}}$ -axis) [9].

IV. CONTROL

The squared rms values of the electric fields in the transverse (x, z) -plane on a test point (sensor location) $\mathbf{q} = (x, z)$ are given by

$$\begin{aligned}\bar{E}_x^2(\mathbf{q}) &= \frac{1}{2} \sum_{\alpha=1}^3 \left(e_\alpha^2 c_\alpha^2 - \sum_{\alpha' > \alpha}^3 c_\alpha c_{\alpha'} e_\alpha e_{\alpha'} \right), \\ \bar{E}_z^2(\mathbf{q}) &= \frac{1}{2} \sum_{\alpha=1}^3 \left(e_\alpha^2 s_\alpha^2 - \sum_{\alpha' > \alpha}^3 s_\alpha s_{\alpha'} e_\alpha e_{\alpha'} \right).\end{aligned}\quad (12)$$

The sum of these quantities provides a closed-form expression for the squared rms magnitude of the electric field

$$\bar{E}^2(\mathbf{q}) = \frac{1}{2} \sum_{\alpha=1}^3 \left(e_\alpha^2 - \sum_{\alpha' > \alpha}^3 c_{\alpha\alpha'} e_\alpha e_{\alpha'} \right) \quad (13)$$

where $c_{\alpha\alpha'} := \cos(\theta_\alpha - \theta_{\alpha'})$. We obtain its gradient using the chain rule resulting in

$$\begin{aligned}\nabla_{\mathbf{q}} \bar{E}^2 &= 2\bar{E} \nabla_{\mathbf{q}} \bar{E} \\ &= \frac{1}{2\xi} \sum_{\alpha=1}^3 e_\alpha \left[\begin{array}{l} -2e_\alpha^2 c_\alpha + \sum_{\alpha' \neq \alpha}^3 e_{\alpha'}^2 \cos(\theta_\alpha - 2\theta_{\alpha'}) \\ 2e_\alpha^2 s_\alpha + \sum_{\alpha' \neq \alpha}^3 e_{\alpha'}^2 \sin(\theta_\alpha - 2\theta_{\alpha'}) \end{array} \right].\end{aligned}\quad (14)$$

Figure 4 indicates that the gradient $\nabla_{\mathbf{q}} \bar{E}$ points into the convex hull of the triangle \mathcal{T} . This is now proven following a lemma.

Lemma 1: Let $\{\hat{\mathbf{f}}_i\}_{i=1}^3$ denote the unit vectors in \mathbb{R}^2 that point from a given location $\mathbf{q} \in \mathbb{R}^2$ to each vertex $\{\mathbf{v}_i\}_{i=1}^3$ of a triangle \mathcal{T} . A vector $\mathbf{v} \in \mathbb{R}^2$ is a conic combination

$$\mathbf{v} = \sum_{i=1}^3 \sigma_i \hat{\mathbf{f}}_i, \quad \sigma_i \geq 0$$

of $\{\hat{\mathbf{f}}_i\}_{i=1}^3$ if and only if the ray it induces $\mathcal{R} \triangleq \{\mathbf{q} + s\mathbf{v} : s \geq 0\}$ intersects the triangle \mathcal{T} .

Proof: It is well-known that a point in the triangle is a convex combination of its vertices. Therefore, the ray \mathcal{R} intersects the triangle \mathcal{T} if and only if the equation

$$\mathbf{q} + s\mathbf{v} = (1 - \beta - \gamma)\mathbf{v}_1 + \beta\mathbf{v}_2 + \gamma\mathbf{v}_3$$

has a solution with $\beta, \gamma, s \geq 0$ and $\beta + \gamma \leq 1$. Rearranging the equation and solving it for \mathbf{v} yields

$$\mathbf{v} = \frac{1}{s}(\mathbf{v}_1 - \mathbf{q}) + \frac{\beta}{s}(\mathbf{v}_2 - \mathbf{v}_1) + \frac{\gamma}{s}(\mathbf{v}_3 - \mathbf{v}_1).$$

Notice that $\mathbf{v}_i - \mathbf{q} = \delta_i \hat{\mathbf{f}}_i$ with $\delta_i \geq 0$ for each $i = 1, 2, 3$. Therefore, this last equation may be rewritten as

$$\mathbf{v} = \frac{\delta_1}{s}(1 - \beta - \gamma)\hat{\mathbf{f}}_1 + \frac{\delta_2}{s}\beta\hat{\mathbf{f}}_2 + \frac{\delta_3}{s}\gamma\hat{\mathbf{f}}_3 \triangleq \sum_{i=1}^3 \sigma_i \hat{\mathbf{f}}_i.$$

Notice that $\sigma_i \geq 0$ for each $i = 1, 2, 3$ due to the constraints on β, γ and s , which was to be demonstrated. ■

Theorem 1: $\nabla_{\mathbf{q}} \bar{E}(\mathbf{q})$ points into the convex hull of \mathcal{T} .

For every $\mathbf{q} \in \mathbb{R}^2$, the gradient $\nabla_{\mathbf{q}} \bar{E}(\mathbf{q})$ points into the convex hull (triangle) of the transmission wires.

Proof: We first show that the gradient is a conic combination of the vectors $\hat{\mathbf{f}}_\alpha := [-c_\alpha \ s_\alpha]^\top$ for $\alpha = 1, 2, 3$. To do so, notice that the expressions in (14) may be equivalently written as

$$\begin{aligned}\nabla_{\mathbf{q}} \bar{E} &= \frac{1}{4\xi \bar{E}} \sum_{\alpha=1}^3 \sigma_\alpha \begin{bmatrix} -c_\alpha \\ s_\alpha \end{bmatrix}, \\ \sigma_\alpha &= e_\alpha \left(\sum_{\alpha'=1}^3 e_{\alpha'}^2 - 2c_{\alpha\alpha'} e_\alpha e_{\alpha'} + e_{\alpha'}^2 \right).\end{aligned}\quad (15)$$

Recall that the vector $\hat{\mathbf{f}}_\alpha = [-c_\alpha \ s_\alpha]^\top$ is the unit vector pointing from the location of a sensor to the α^{th} transmission wire. We can readily see that $\sigma_\alpha \geq 0$ for all $\alpha = 1, 2, 3$. Indeed, $e_\alpha > 0$ and

$$\begin{aligned}e_\alpha^2 - 2c_{\alpha\alpha'} e_\alpha e_{\alpha'} + e_{\alpha'}^2 &= \begin{bmatrix} e_\alpha & e_{\alpha'} \end{bmatrix} Q \begin{bmatrix} e_\alpha \\ e_{\alpha'} \end{bmatrix} \geq 0, \\ Q &= \begin{bmatrix} 1 & -c_{\alpha\alpha'} \\ -c_{\alpha\alpha'} & 1 \end{bmatrix} \succeq 0.\end{aligned}$$

Here \succeq denotes that the matrix is positive semidefinite, which can be deduced by computing its principal minors. Therefore, we see that $\sigma_\alpha \geq 0$ for all α . ■

Remark 1: If the triangle \mathcal{T} does not degenerate into a line segment, not all $\{\theta_\alpha\}_{\alpha=1}^3$ can be equal, implying that there exists an α such that $\sigma_\alpha > 0$. This follows from the above computation of the matrix Q , which is positive definite unless $\theta_\alpha = \theta_{\alpha'}$, with $\alpha \neq \alpha'$.

Remark 2: The fact that the $\nabla_{\mathbf{q}} \bar{E}$ points into the triangle \mathcal{T} formed by the transmission wires implies, in particular, that the critical points of \bar{E} lie in the (closed) triangle. Consequently, the unit vector along the $\nabla_{\mathbf{q}} \bar{E}$ may be used as a bearing factor with respect to which localization may be performed.

Remark 3: Substituting from equation (11) into equation (13) we obtain

$$\bar{E}^2(\mathbf{q}) = \frac{\xi^2}{2} \sum_{\alpha=1}^3 \left(\frac{1}{r_\alpha^2} - \sum_{\alpha' > \alpha}^3 \frac{c_{\alpha\alpha'}}{r_\alpha r_{\alpha'}} \right).$$

This implies that $\bar{E}^2(\mathbf{q}) = O(1/r_\alpha^2)$ as $r_\alpha \rightarrow 0$ for some $\alpha = 1, 2, 3$. In this sense, a measure of the “distance” to the power lines is provided by ξ/\bar{E} .

A. Potential Function

We define a potential function $V : \mathbb{R}^2 \rightarrow \mathbb{R}_+$ as follows

$$V(\mathbf{q}) \triangleq \frac{1}{\bar{E}^2(\mathbf{q})}. \quad (16)$$

This is a continuously differentiable, nonnegative, decreasing function of \bar{E} , with a global minimum value of zero at $r_\alpha = 0$ for each $\alpha = 1, 2, 3$. Taking the gradient of V , we see that

$$\nabla_{\mathbf{q}} V(\mathbf{q}) = -\frac{2}{\bar{E}^3} \nabla_{\mathbf{q}} \bar{E}(\mathbf{q}) = -\frac{1}{2\xi \bar{E}^4} \sum_{\alpha=1}^3 \sigma_\alpha \hat{\mathbf{f}}_\alpha. \quad (17)$$

Since each σ_α is a third-order polynomial of peak electric field strengths e_α , the magnitude of the gradient $\|\nabla_{\mathbf{q}} V(\mathbf{q})\| = O(1/\bar{E})$ as $\bar{E} \rightarrow \infty$ (equivalently as $r_\alpha \rightarrow 0$ for some α).

B. Behavior of the Critical Points of the Potential Function

The negative gradient $-\nabla_q V$ of V points into the triangle \mathcal{T} , therefore by Remark 2, we know that it may only vanish within \mathcal{T} . In particular, by equations (16), (17) the gradient of $V(q)$ vanishes as $e_\alpha \rightarrow \infty$ ($r_\alpha \rightarrow 0$) for some α .

The critical points of V are the zeros of $\nabla_q V(q)$. However, the right-hand-side of equation (17) is written in terms of the variables $\{e_\alpha, \theta_\alpha\}_{\alpha=1}^3$ rather than $q = (x, z)$. In order to locate the critical points in terms of $\{e_\alpha, \theta_\alpha\}_{\alpha=1}^3$, we develop four additional constraints based on the geometry these variables must satisfy. Specifically, the trivial vector loop equations

$$q - v_\alpha + v_{\alpha+1} - q = v_{\alpha+1} - v_\alpha, \quad \alpha = 1, 2. \quad (18)$$

which may equivalently be written as

$$\frac{\xi}{e_\alpha} \begin{bmatrix} c_\alpha \\ -s_\alpha \end{bmatrix} - \frac{\xi}{e_{\alpha+1}} \begin{bmatrix} c_{\alpha+1} \\ -s_{\alpha+1} \end{bmatrix} = \begin{bmatrix} x_{\alpha+1} - x_\alpha \\ z_{\alpha+1} - z_\alpha \end{bmatrix}, \quad \alpha = 1, 2.$$

Now we have 6 equations to solve for the 6 unknowns $\{e_\alpha, \theta_\alpha\}_{\alpha=1}^3$. Simultaneously solving

$$\nabla_q V(q) = -\frac{1}{2\xi E^4} \sum_{\alpha=1}^3 \sigma_\alpha \hat{f}_\alpha = \mathbf{0}$$

along with the loop equations (18) provides us with the critical points of the potential function V . Let us coin the term *generic* for a triangle that is sufficiently far away from being equilateral. It turns out that unless \mathcal{T} is “almost” equilateral, i.e., generic, then there are five critical points. Three of these five occur at the location of the power lines (vertices of the triangle \mathcal{T}) and are global minima with a zero value. The remaining critical points have to be saddle points of V , which is our next result.

Lemma 2: Let the triangle \mathcal{T} be generic and V have isolated critical points. Then the remaining two critical points of the potential function V are saddle points.

Proof: The Euler characteristic of a triangle is

$$\chi(\mathcal{T}) = V - E + F = 3 - 3 + 1 = 1.$$

By Poincaré-Hopf theorem [11], we know that the sum of the indices of the gradient vector field of V equals this integer. Since the global minima of V are sinks, they have indices of +1. This implies that the index of the remaining two critical points must sum to -2. As long as these two critical points are not located at the same spatial location with multiplicity two, they must each have index -1, implying that they are saddle points of V . ■

Remark 4: If \mathcal{T} is not generic, there are 7 critical points. The first three are the same as before, i.e., the location of the power lines. The remaining four contain three saddle points and a maximum. Each of the saddle points contributes -1 to the index sum, while the maximum contributes a +1, as demanded by the Poincaré-Hopf theorem: $3 - 1 - 1 - 1 + 1 = 1 = \chi(\mathcal{T})$.

When we compute the Hessian $H_V(q)$ of V and take the limit as $r_\alpha \rightarrow 0$, the Hessian becomes positive definite.

$$\lim_{r_\alpha \rightarrow 0} H_V(q) = 4/\xi^2 I, \quad \alpha = 1, 2, 3,$$

where I is the identity matrix, verifying that the power lines are minima of V . In fact, they are the global minima since V equals zero at these locations and $V(q) \geq 0$ for all $q \in \mathbb{R}^2$.

C. UAV Control Using Gradient Flow

Section IV-B shows that the potential function V has maxima at the desired locations, i.e., where the power lines are located in the $q = (x, z)$ -plane. The same section describes the fact that it has no other minima in this domain. As we show in this subsection, this implies that following the gradient vector field in the q -plane will take the drone to one of the power lines.

Suppose that the drone's equations of motion are (partially) feedback linearized so that its motion in the q -plane is governed by

$$\ddot{q} = u, \quad (19)$$

where u is the control input. Consider the damped, gradient-based control law

$$u(q, \dot{q}) = -k_p \nabla_q V(q) - k_d \dot{q}. \quad (20)$$

Under this control input, we show that essentially $q \rightarrow q_\alpha^*$, where q_α^* corresponds to $r_\alpha = 0$ (one of the power line locations) for some $\alpha = 1, 2, 3$.

Consider the Lyapunov function candidate

$$W(q, \dot{q}) = k_p V(q) + \frac{1}{2} \dot{q}^\top \dot{q},$$

which is positive definite¹ and is equal to zero if and only if $q = q_\alpha^*$. Its derivative along the trajectories of the double integrator system under the control law (20) is given by

$$\dot{W} = (k_p \nabla_q V(q) + u)^\top \dot{q} = -k_d \|\dot{q}\|^2 \leq 0,$$

which vanishes in the set $E = \{(q, \dot{q}) \in \mathbb{R}^4 : \dot{q} \equiv \mathbf{0}\}$. The largest positively invariant set $M \subseteq E$ is seen to be $M = \{(q, \dot{q}) : (\nabla_q V(q), \dot{q}) = \mathbf{0}\}$, that is, M is characterized by the critical points of V . This is because if $\nabla_q V(q) \neq \mathbf{0}$ and $\dot{q} = \mathbf{0}$, then equations (19), (20) imply $\ddot{q} \neq \mathbf{0}$ and hence this particular state is not positively invariant. Points that satisfy $\nabla_q V(q) = \mathbf{0}$ were characterized in Section IV-B to consist of three sinks ($r_\alpha = 0$), and potentially 2 or 3 saddle points and 1 source. The closed-loop system (19), (20) is unstable except at the locations where $r_\alpha = 0$. To show this, consider the linearization of the closed-loop system near a source or a saddle point q_s :

$$\begin{bmatrix} \delta \dot{q} \\ \delta \ddot{q} \end{bmatrix} = A \begin{bmatrix} \delta q \\ \delta \dot{q} \end{bmatrix} = \begin{bmatrix} \mathbf{0} I \\ -k_p H_V(q_s) - k_d I \end{bmatrix} \begin{bmatrix} \delta q \\ \delta \dot{q} \end{bmatrix}. \quad (21)$$

The Hessian $H_V(q_s)$ of V is sign indefinite if q_s is a saddle point, and is negative definite if q_s is a source, neither of which makes A a Hurwitz matrix. Hence, the set of initial conditions from which the closed-loop system approaches these unstable equilibria does not have an interior. Therefore, a real implementation of a UAV cannot reach these points.

¹ $V > 0$ except at $r_\alpha = 0$ for some $\alpha = 1, 2, 3$.

TABLE I
PARAMETERS OF THE SIMULATION ENVIRONMENT

I_0 [A]	β	Power Line Separation [m]	Sensor noise std.
700	9/10	5	1/1000

1) *Choosing the Gains k_p and k_d* : The linearization of the closed-loop system given in equation (21) holds at $\mathbf{q} = \mathbf{q}_\alpha^*$ with $\mathbf{H}_V(\mathbf{q}_\alpha^*) = 4/\xi^2 \mathbf{I}$, as computed in Section IV-B. Its characteristic polynomial is computed as

$$p_c(s) = \left(s^2 + k_d s + \frac{4k_p}{\xi^2} \right)^2.$$

In order to place the (double) roots of the linearized closed-loop system at $r_1, r_2 < 0$, we set $k_d = -(r_1 + r_2)$ and $k_p = \frac{\xi^2}{4} r_1 r_2$.

Remark 5: One needs to be able to compute the gradient of V in order to be able to apply this control law. The gradient is estimated numerically by mounting multiple electric/magnetic field sensors at known locations on the UAV.

Remark 6: Unless it is approximated by some other means, we may not have knowledge of ξ , needed to perform exact pole placement.

2) *Magnetic Field Measurements*: As the contour lines of the rms magnetic and electric fields are the same, the potential V in equation (16) may be equivalently expressed using the rms magnetic field magnitude: $V(\mathbf{q}) = 1/\bar{B}^2(\mathbf{q})$.

V. CASE STUDY

We provide a case study on how the control law devised in Section IV would be used on a UAV to navigate to a power line. The gradient term in the control law (20) will be computed by electric/magnetic field sensors mounted on the drone. The damping term that involves the velocity $\dot{\mathbf{q}}$ will be typically computed using GPS measurements. Note that the GPS cannot provide the relative distance to a power line, however, $\dot{\mathbf{q}}$ is equal to the relative velocity since the power line does not move.

By choosing the gains k_p and k_d appropriately, the trajectory in the configuration space (\mathbf{q} -space) will follow the gradient vector field of V . Specifically, we want the reference velocity to satisfy $\dot{\mathbf{q}}_{\text{ref}} = -\tilde{k}_p \nabla_{\mathbf{q}} V(\mathbf{q})$. Now, to have the system velocity to follow $\dot{\mathbf{q}}_{\text{ref}}$, set the acceleration to

$$\ddot{\mathbf{q}} = \mathbf{u} = -k_d(\dot{\mathbf{q}} - \dot{\mathbf{q}}_{\text{ref}}) = -k_d \dot{\mathbf{q}} - k_d \tilde{k}_p \nabla_{\mathbf{q}} V(\mathbf{q}).$$

To ensure that $\dot{\mathbf{q}} \rightarrow \dot{\mathbf{q}}_{\text{ref}}$ fast requires taking a large enough k_d (high-gain feedback).

Figure 6 shows a UAV converging under this control law to one of the three-phase power lines. Note that the trajectory in the configuration space follows the gradient of V . The parameters used for the simulation environment is provided in Table I.

VI. CONCLUSION

We have provided a procedure to stably navigate a UAV around a three-phase power line. This type of stable locomotion and manipulation is required for tasks such as bird-diverter

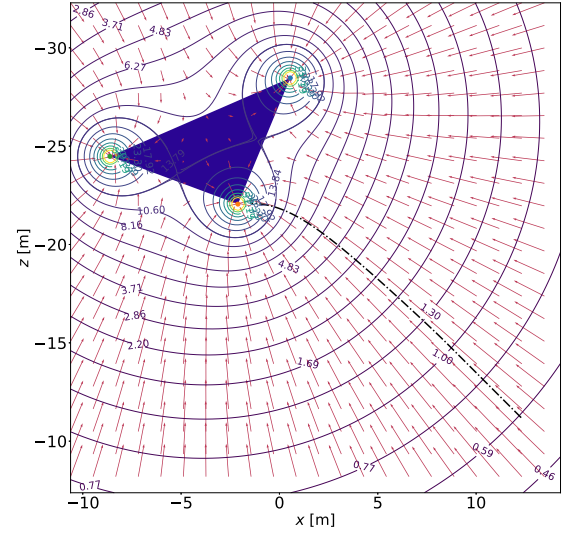


Fig. 6. Sample trajectory of a UAV under the control strategy provided in Section IV. The dash-dotted black line depicts the motion of the UAV in the (x, z) -plane. Note that the trajectory follows the gradient of V .

and dynamic line-rating sensor installations. We showed that the squared reciprocal of the total rms electric or magnetic field magnitudes serve as potential functions, whose gradient may be followed to reach one of the power lines on a balanced three-phase system. The control algorithm developed in Section IV is implemented in simulation with success, supporting the efficacy of the method. We are currently working on implementing this control strategy on Pitch Aeronautics's cyclorotor-based UAV, Astria [12].

REFERENCES

- [1] B. P. Bhattarai et al., "Improvement of transmission line ampacity utilization by weather-based dynamic line rating," *IEEE Trans. Power Del.*, vol. 33, no. 4, pp. 1853–1863, Aug. 2018.
- [2] T. O. Seppa, "Power transmission line tension monitoring system," U.S. Patent 5 517 864, May 1996.
- [3] A. Michiorri et al., "Forecasting for dynamic line rating," *Renew. Sustain. Energy Rev.*, vol. 52, pp. 1713–1730, Dec. 2015. [Online]. Available: <https://www.sciencedirect.com/science/article/pii/S1364032115007819>
- [4] M. Schwarz and D. Drudi, "Workplace hazards facing line installers and repairers," *Month. Lab. Rev.*, vol. 141, p. 1, Feb. 2018.
- [5] Pitch Aeronautics, Astria. *Abstract Liquid Background Video (No Sound)-4K UHD Abstract Liquid Screensaver*. [Online Video]. Available: https://youtu.be/S9F0jz4eqNY?si=0ZHaIQg_vOa6v88
- [6] Pitch Aeronautics, Astria. [Online Video]. Available: https://youtu.be/aBcJUUR_Tk
- [7] K. Kaiser, *Transmission Lines, Matching, and Crosstalk*. Oxfordshire, U.K.: Taylor & Francis, 2005. [Online]. Available: <https://books.google.com/books?id=QWFD-33xXvgC>
- [8] R. G. Olsen and P. S. K. Wong, "Characteristics of low frequency electric and magnetic fields in the vicinity of electric power lines," *IEEE Trans. Power Del.*, vol. 7, no. 4, pp. 2046–2055, Oct. 1992.
- [9] R. K. Wangsness, *Electromagnetic Fields*. New York, NY, USA: Wiley, 1979.
- [10] R. Harrington, *Time-harmonic Electromagnetic Fields* (Electronics Series). New York, NY, USA: McGraw-Hill, 1961. [Online]. Available: <https://books.google.com/books?id=FtpPAAAAAAAJ>
- [11] K. Burns and M. Gidea, *Differential Geometry and Topology: With a View to Dynamical Systems* (Studies in Advanced Mathematics). Oxfordshire, U.K.: Taylor & Francis, 2005. [Online]. Available: <https://books.google.com/books?id=tV9sTDnaf40C>
- [12] "Pitch Aeronautics." pitchaero.com. 2022. [Online]. Available: <https://www.pitchaero.com/>